Electronic Supplementary Information

Flexible iontronics with super stretchability, toughness and enhanced conductivity based on collaborative design of high-entropy topology and multivalent ion-dipole interactions

Wang Zhan [a #], Jianrui Zhang [b #], Qi Zhang [c,d], Zhilu Ye [a], Boyang Li [b], Cuiling Zhang [a], Zihao Yang [a], Li Xue [a], Zeying Zhang [a], Feng Ma [b], Niancai Peng [e], Yi Lyu [b], Yaqiong Su [d], Ming Liu [d*], Xiaohui Zhang [a*]

[a] State Key Laboratory for Manufacturing Systems Engineering, The Key Laboratory of Biomedical Information Engineering of Ministry of Education, Center for Mitochondrial Biology and Medicine, School of Life Science and Technology, International Joint Laboratory for Micro/Nano Manufacturing and Measurement Technology, Xi'an Key Laboratory for Biomedical Testing and High-end Equipment, Xi'an Jiaotong University, Xi'an 710049, Shannxi, P.R. China.

[b] School of Chemistry, Engineering Research Center of Energy Storage Materials and Devices of Ministry of Education, National Innovation Platform (Center) for Industry-Education Integration of Energy Storage Technology, Xi'an Jiaotong University, Xi'an, 710049, China

[c] National Local Joint Engineering Research Center for Precision Surgery & Regenerative Medicine, Shaanxi Provincial Key Laboratory of Magnetic Medicine, Department of Hepatobiliary Surgery, The First Affiliated Hospital of Xi'an Jiaotong University, No. 277 West Yanta Road, Xi'an, 710061, Shaanxi, China.

[d] State Key Laboratory for Manufacturing Systems Engineering, Electronic Materials Research Laboratory, Key Laboratory of the Ministry of Education, Engineering Research Center of Spin Quantum Sensor Chips, Universities of Shaanxi Province, School of Electronic Science and Engineering, Xi'an Jiaotong University, Xi'an 710049, China.

[e] State Key Laboratory for Manufacturing Systems Engineering, School of Instrument Science and Technology, International Joint Laboratory for Micro/Nano Manufacturing and Measurement Technology, Xi'an Key Laboratory for Biomedical Testing and High-end Equipment, Xi'an Jiaotong University, Xi'an 710054, China.

* Corresponding author.

E-mail address: mingliu@xjtu.edu.cn (M. Liu); xiaohuizhang@mail.xjtu.edu.cn (X. Zhang).

# Equal contribution.

Contents

1. Materials and Methods

1.1 Materials

The granules of polyester-based thermoplastic polyurethane (TPU, HF2385A) were procured from Zhejiang Huafon TPU Co., Ltd in China. Tetrahydrofuran (THF), Bis(trifluoromethane)sulfonimide lithium salt (LiTFSI), N, N-Dimethylformamide (DMF), Polyethylene glycol (PEG) with average molecular weights of 200, 1500, 4000 and 20000, Isophorone diisocyanate (IPDI) and Dibutyltin dilaurate (DBTDL) were procured from Shanghai Macklin Biochemical Co., Ltd. in China. All the chemicals were analytical reagents and used directly without any further purification.

1.2 Synthesis of ASSICEs

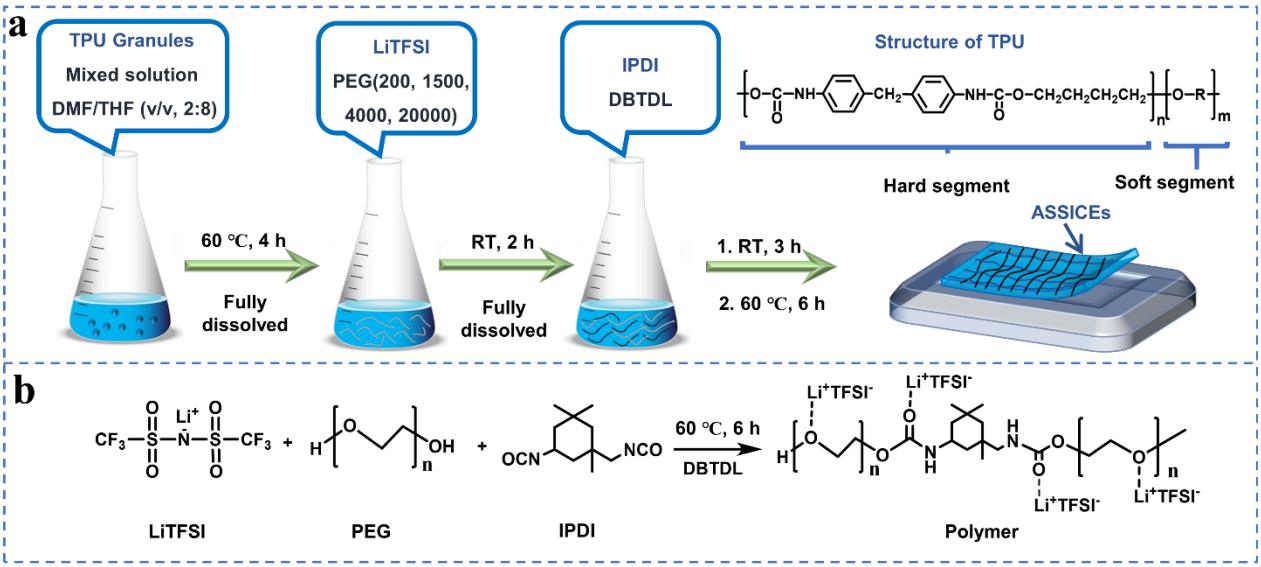

Fig. S1 Fabrication process of the all-solid-state ionic conductive elastomer. (a) Fabrication process of the ASSICEs and the chemical structure of commercial thermoplastic polyurethane (TPU). (b) The extension of PEG molecule chains and the interaction between Li^+ ions and polymer matrix chains.

The ASSICEs were synthesized using a facile solvent casting method (Fig. S1). Taking the specimen TLP_{20000} as an example, the TPU granules (2.00g) completely

dissolved in a mixed solution of DMF/THF (v/v, 2/8) (10 mL) under the condition of reflux with a condensation temperature of 60 ℃. The solution was then cooled to room temperature under an airtight condition. Then, PEG_{20000} (0.20g) and LiTFSI (1.00g) were completely dissolved in as-prepared solution with the aid of ultrasonic and eddy oscillations. Subsequently, IPDI crosslinker (0.20 mL) and DBTDL catalyst (0.025 mL) were introduced with vigorous mixing and ultrasonic degassing before being poured into Teflon molds for room temperature pre-polymerization lasting 3 hours. Finally, The ASSICEs were obtained by subjecting the Teflon molds to a temperature of 60 ℃ for a duration of 6 hours. Additionally, a series of control groups for ASSICEs were synthesized and their formulations are presented in Table S2.

1.3 Characterization Methods of ASSICEs

A universal tensile testing machine (CMT1502, Sansi, China) equipped with a 50 N load cell was utilized to evaluate the mechanical properties of ASSICEs at a tensile speed of 50 mm/min. The tensile strain (ε) was defined as the length change (Δl) divided by the original length (l_0) of the specimen. The toughness was calculated by integrating the area under the fracture curve with respect to the X-axis. The Young's modulus was calculated through regression analysis of the initial linear segment (ranging from 5% to 20% elongation) in the stress-strain curve. The dissipation of energy was defined as the integration of the average polygonal area over 50 cycles under a tensile strain of 100%.

The electrical properties of ASSICEs were evaluated using a universal testing machine and LCR meter (TH2832, Tonghui, China). The conductivity (σ, S/m) was

defined as the quotient of the distance (L, m) between two electrodes and the product of electrode area (S, m^2) and resistance (R, Ω). The relative resistance variation ($\Delta R/R_0$) was defined as relative resistance change (R-R_0) under a specific strain divided by the original resistance (R_0). The sensitivity of the specimen is expressed as GF and defined as the ratio of relative resistance variation ($\Delta R/R_0$) to tensile strain (ε). The characterized samples were prepared with 5 parallel controls.

The glass-transition temperature of ASSICEs was evaluated using differential scanning calorimeter (DSC250, TA, USA). The procedure was conducted as follows: the samples (5-10 mg) were hermetically sealed in an aluminum pan and ramped from −100 ℃ to 100 ℃ at a rate of 20 ℃ min^{-1} under a nitrogen atmosphere.

The interaction between ASSICEs networks was analyzed via Micro-Infrared Spectroscopy (MIR), which were acquired using a spectrometer (VERTEX 70, Bruker, USA) and measured over a frequency range between 400 and 4000 cm^{-1}. The temperature was maintained at 25 ℃ during the test.

X-Ray Diffraction (XRD, Bruker D8 ADVANC, GER.) were employed to investigate the microstructure of the sample at a scanning range of 5°-80°.

The element distribution and morphology of ASSICEs were characterized using a Scanning Electron Microscope (SEM, Gemini 500, GER). Prior to testing, the specimens were subjected to gold spraying.

The Raman spectra of the ASSICEs were recorded by a Raman spectrometer (LabRAM Aramis, HORIBA, France) using a 532 nm laser and measured over a

frequency range between 400 and 4000cm^{-1}. The temperature was maintained at 25 ℃ during the test.

The 3D morphology of the ASSICEs' surface was measured using a laser confocal surface roughness measurement system (Optical surface measurement system, Leica DCM8, GER.).

The residual DMF was assessed via high-performance liquid chromatography (HPLC) (Thermo, U3000, USA). HPLC analytical methods of residual DMF: (1) Control group: a certain mass of DMF solution was completely dissolved in methanol to obtain a control solution, which served as a standard (0.248mg/mL). (2) Leaching solution of ASSICEs: the solid film weighing 0.315g was fragmented into small pieces, followed by the addition of 3mL methanol for ultrasonic extraction lasting 1 hour. Subsequently, HPLC was employed for detection. (3) Detection conditions of HPLC: the mobile phase comprised pure methanol, with a flow rate of 1 mL/min. An injection volume of 10 μL was utilized, and detection at 263 nm was performed using a UV detector.

1.4 Applications of ASSICEs

As a proof of concept, the ASSICEs we have developed at the laboratory level demonstrates potential applications as a strain sensor in various fields, including human-machine interface communication, vacuum measurement in aerospace, and medical balloon monitoring for medical devices. For the purpose of human-machine interface communication, we prepared rectangular samples (5 mm × 20 mm) by cutting the

original specimens (40 mm × 40 mm), attaching two copper electrodes to each end of the samples, and securing them onto the second joint of the right index finger with electrical tape. Similarly, we attached one end of the strain sensor to the piston cylinder of the syringe in which was hermetically sealed with a small amount of air, and the other end was linked to the piston handle for vacuum measurement. Additionally, we affixed the strain sensor onto the surface of a medical balloon model and subsequently placed it within a centrifuge tube to evaluate the extent of balloon expansion. Written informed consent was obtained from all participants' parents or surrogate decision makers prior to the research. This study was review and approved by the Institutional Review Board Committee of Medical College of Biology (2019-23), Xi'an Jiaotong University, Xi'an Shaanxi.

1.5 Chemical model construction and calculation

The computations outlined in this study were executed using the Gaussian 16 suite of programs. Geometries for both isolated ions and ionic pairs within the investigated systems were meticulously optimized without any imposition of symmetry constraints. For these optimizations, the hybrid functional B3LYP in conjunction with the 6-311++G(2d,2p) basis set with an empirical dispersion correction term (DFT-D3) was employed [1-4]. Furthermore, for the visualization of all simulations, the VMD software was utilized [5]. The binding energy (E_b) was calculated via the following equation:

$$E_b = E_{total} - E_{PEG} - E_{Li}$$

where the E_{PEG} is the energy of the PEG, the E_{Li^+} is the energy of Li^+ and the E_{total} is the total energy after adsorption.

The Gibbs free energies at 298.15 K and 1 atm were calculated with

$$G = H - TS = E_{DFT} + E_{ZPE} + \int_0^{298.15K} C_p dT - TS$$

where E_{DFT} is the total energy obtained from DFT optimization, E_{ZPE} is the zero-point vibrational energy, C_p is the heat capacity, T is the kelvin temperature, and S is the entropy.

The topological analysis of ASSICEs was carried out using the Z1+ code package reported by Kröger [6]. Utilizing the coarse-graining model, we generated the structural configuration of the copolymer melt and subsequently analyzed its entanglement number.

2. Supporting Note 1. All Related Tables of ASSICEs

Table S1. Comprehensive performance comparison of ASSICEs.

Elastomer composition	Ionic conductivity (S/m)	Fracture strain (%)	Toughness (MJ/m^3)	Breaking strength (MPa)	References
PTMEG/HEDS-Upy/LiTFSI	1.85×10^{-3} at 30℃	2632	61.77	6	7
PEGDA575/MEA/SiNPs/LiTFSI	10^{-3} S/m	225	8.6	4.3	8
PTFEA-co-PFOEA/LiTFSI	10^{-6} S/m	2168	-	-	9
IP6/PVA	3.3×10^{-2} S/m at 25℃	573	-	12.5	10
Uio-66-NH-MET/PETMP/PEGMA/LiTFSI	2.26×10^{-2} at 25℃	500	-	9.4	11
Jeffamine D400 /Jeffamine T403 /adipic acid/LiTFSI	2.5×10^{-2} at 25℃	130	0.32	0.15	12
ACMO/TTEGDA/1-Butyl-3-methylimidazolium Bis(trifluoromethylsulfonyl)imide ([BMIM][TFSI]	7×10^{-3} at 25℃	300	-	-	13
IBA/MEA/LiTFSI	5.28×10^{-3} at 25℃	1640	0.02	7	14
PIL/TFSI	1.31×10^{-2} at 25℃	540	-	0.24	15
RM257/EDDET/PETMP	1.4×10^{-4}S/m	2700	56.9	4.7	16
BA/PEGDA/LiTFSI	1.27×10^{-5} S/m at 20℃	1100	-	0.25	17
PTMEG/HEDS/Upy/LiTFSI	3.77×10^{-3} S/m at 30℃	2615	164.36	27.83	18
DC-PEO/LiTFSI	2.04×10^{-2} S/m at 25℃	563	-	0.3	19
AETATFSI/BzA/OEGA	1.5×10^{-4} at 25℃	1521	-	0.64	20
TPU/PEG/LiTFSI	**1.15×10^{-2} S/m, 25℃**	**2621**	**107.19**	**7.45**	**Our work**

We conducted a comprehensive performance comparison of ASSICEs in the Table S1, the result shows that the ionic conductivity and fracture strain of ASSICEs in our work exhibit an absolute advantage. Besides, the ASSICEs also possess significant

advantages, as evidenced by a sample evaluation of their preparation method and cost. This implies that the fabrication method and strategy can be easily scaled up and industrialized.

Table S2. Content of main materials used in the synthesis of the samples.

Elastomers	TPU granules (g)	PEG (g)	LiTFSI (g)	IPDI (mL)	DBTDL (mL)	DMF/THF solution (v/v, 2/8) (mL)
TPU	2	0	0	0	0	10
TL	2	0	1	0	0	10
TLP_{200}	2	0.2	1	0.20	0.025	10
TLP_{1500}	2	0.2	1	0.20	0.025	10
TLP_{4000}	2	0.2	1	0.20	0.025	10
TLP_{20000}	2	0.2	1	0.20	0.025	10

In order to successful fabricate the ASSICEs film, we firstly prepared the mother liquor by dissolving TPU granules into the mixture solution (DMF/THF, 2/8, v/v), then dissolved the PEG, LiTFSI, IPDI and DBTDL, next, got the sample by casting the mixed solution into the Toflon model and one-step condensation polymerization.

Table S3. The determination of binding energy, Gibbs free energy, and entropy values utilizing density functional theory (DFT).

Degree of Polymerization	Li^+-PEG_1	Li^+-PEG_3	Li^+-PEG_6	Li^+-PEG_9	Li^+-PEG_{12}	Li^+-PEG_{15}
Binding Energy (ΔE, $kJ \cdot mol^{-1}$)	-174.56	-390.07	-571.58	-590.13	-635.89	-733.32
Gibbs free energy (ΔG, $kJ \cdot mol^{-1}$)	-140.56	-338.41	-508.84	-533.15	-553.13	-619.52
Entropy value (S, cal/K·mol)	78.47	111.03	156.75	206.57	316.55	382.55

The binding energy, Gibbs free energy and entropy values between Li^+ and single PEG molecule with varying degrees of polymerization was calculated using the density

functional theory, the detailed data are shown in the Table S3. The entropy can be calculated from the binding energy and Gibbs free energy, and the entropy increases with the increase of the degree of polymerization of PEG. Therefore, in our ionic conductive elastomer system, the degree of polymerization of PEG can reach about 900, thereby enabling the material to attain a high level of entropy.

Table S4. The binding energy, Gibbs free energy and entropy values between Li^+ and 2 PEG molecules with varying degrees of polymerization.

Degree of Polymerization	Li^+-PEG_3-PEG_1	Li^+-$2PEG_3$	Li^+- PEG_3-PEG_6	Li^+- PEG_3-PEG_9	Li^+- PEG_3-PEG_{12}	Li^+- PEG_3-PEG_{15}
Binding Energy (ΔE, $kJ \cdot mol^{-1}$)	-421.77	-468.20	-633.37	-839.32	-895.43	-918.76
Gibbs free energy (ΔG, $kJ \cdot mol^{-1}$)	-342.24	-414.92	-598.19	-765.87	-818.22	-843.47
Entropy value (S, cal/K·mol)	149.7	179.86	203.99	261.28	321.14	366.93

Table S5. The binding energy, Gibbs free energy and entropy values between Li^+ and 3 PEG molecules with varying degrees of polymerization.

Degree of Polymerization	Li^+-$2PEG_3$-PEG_1	Li^+-$3PEG_3$	Li^+- $2PEG_3$-PEG_6	Li^+- $2PEG_3$-PEG_9	Li^+- $2PEG_3$-PEG_{12}	Li^+- $2PEG_3$-PEG_{15}
Binding Energy (ΔE, $kJ \cdot mol^{-1}$)	-816.65	-851.00	-900.80	-942.19	-1188.40	-1227.80
Gibbs free energy (ΔG, $kJ \cdot mol^{-1}$)	-798.41	-812.05	-882.94	-908.26	-1059.39	-1186.00
Entropy value (S, cal/K·mol)	214.30	222.18	262.95	322.95	353.17	506.04

The binding energy, Gibbs free energy, and entropy values between Li+ and multiple PEG molecules (e.g., 2 and 3 PEG molecules) are presented in Table S4 and Table S5.

The results indicate that in the presence of multiple PEG molecules, the binding energy, Gibbs free energy, and entropy values continues to increase with the degree of polymerization.

Table S6. Comparison of comprehensive properties of ASSICEs for iontronics.

Ionic conductive elastomers	Stretchability (%)	Ionic conductivity (S/m)	Sensitivity	References
P(MEA-co-IBA)/LiTFSI	1640	5.28×10^{-3} at 25℃	2.02(1%), 4(100%), 6(200%)	14
P(BS-co-MEA) /LiTFSI	100	3.4×10^{-3} ~ 2.6×10^{-2}	0.51(0-50%)	21
P(IA/AA/DMA)	559	2×10^{-2} ~ 4×10^{-2}	1.736(0-100%), 3.038(100%-200%), 4.172(200%-300%)	22
PIL-PDES([ATAC][TFSI]/AA/ChCl)	760	2.49×10^{-3}	1.95(0-100%), 1.94(100%-300%), 2.5(300%-500%)	23
P(AA/ChCl/PEGDA)	2100	2.33×10^{-2}	0.69(0-200%), 2.75(200%-600%), 3.54(600%-1000%)	24
PHFBA-r-OEGA/LiTFSI	>6000	3.5×10^{-3}	1.0(0-350%)	25
WPU/mHNTs/[EMIM][TFSI]	1069	1.85×10^{-1}	1.28(0-100%), 2.31(100%-400%)	26
PLA/LiTFSI	1585	2.14×10^{-5}	0.64(0-1000%), 1.15(1000%-1500%)	27
LA/ChCl	823	1.05×10^{-3}	1.53(0-100%), 2.96(100%-500%), 3.83(500%-800%)	28
TPU/PEG/LiTFSI	**2621**	**1.15×10^{-2}, 25℃**	**1.92(0-200%), 3.29(200%-1000%)**	**Our work**

In addition to the comprehensive comparison of ASSICEs detailed in Table S2, we have extended our investigation by incorporating them into a strain sensor and conducting a comprehensive assessment of the sensor's tensile properties, ionic conductivity, and sensitivity. As delineated in Table S6, the developed ASSICE-based

strain sensor exhibits significant advantages in these three essential sensing properties. The excellent sensing properties can be attributed to our innovative collaborative design, which combines a high-entropy topological network for superior mechanical properties with polyvalent ion-dipole interactions, providing a foundation for outstanding ionic conductivity. The synergistic effect of these two factors underlies the remarkable sensitivity and environmental robustness (including temperature and humidity resistance) exhibited by the strain sensor.

3. Supporting Note 2. Characterization Results and Discussion of ASSICEs

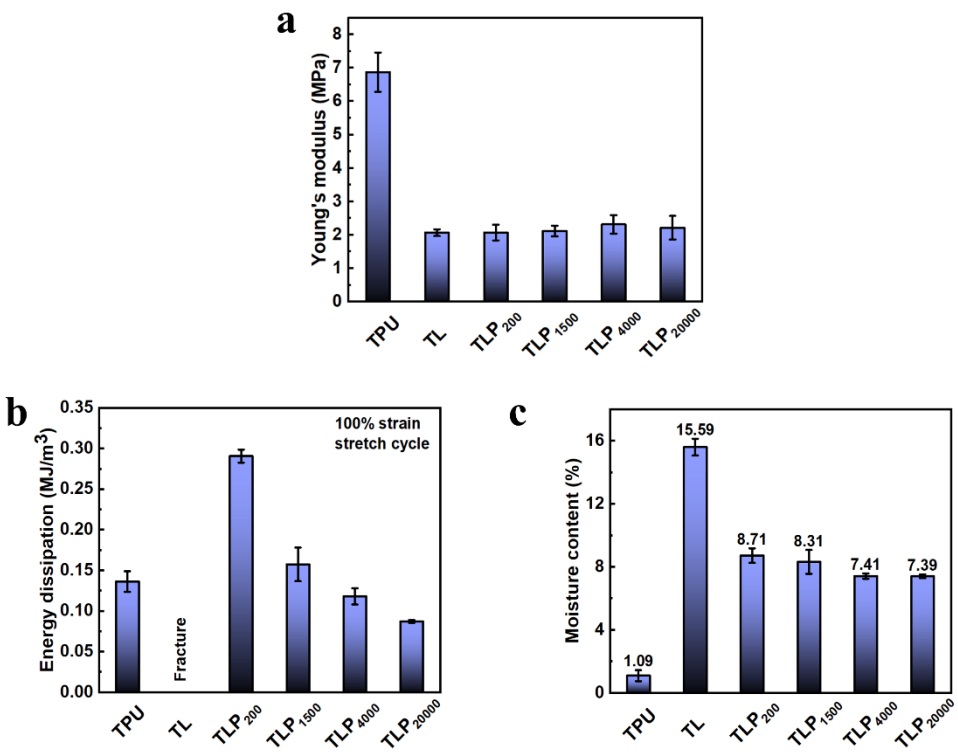

Fig. S2 (a) Young's modulus of various samples. (b) Energy dissipation of various samples. (c) Moisture content of various samples.

Yong's modulus is a very important index of material flexibility, representing whether it can completely fit different surfaces. The results presented in Fig. S2a demonstrate that the incorporation of LiTFSI and PEG_{20000} into the TPU matrix leads to a Yong's modulus of approximately 2 MPa, rendering it more suitable for effective fit to various surfaces of the human body. The energy dissipation is a presentation of the resilience of the elastomer. The smaller the energy dissipation, the stronger the recovery ability after the shape change of the elastomer. Fig. S2b shows that the sample with LiTFSI and PEG_{20000} possess the lowest energy dissipation, that means the formation of topological structure between TPU and PEG_{20000}. The moisture of various sample as

depicted in Fig. S2c. The sample of pure TPU containing LiTFSI exhibit more high moisture, demonstrating that LiTFSI absorb a lot of water due to fewer ether and ester groups on the TPU chain are unable to fully couple with lithium ions. Conversely, when introduction the PEG that containing lots of ethoxy groups to the TPU elastomer matrix, all the Li^+ almost being coupling with ethoxy groups and great reduce the ability to absorb water.

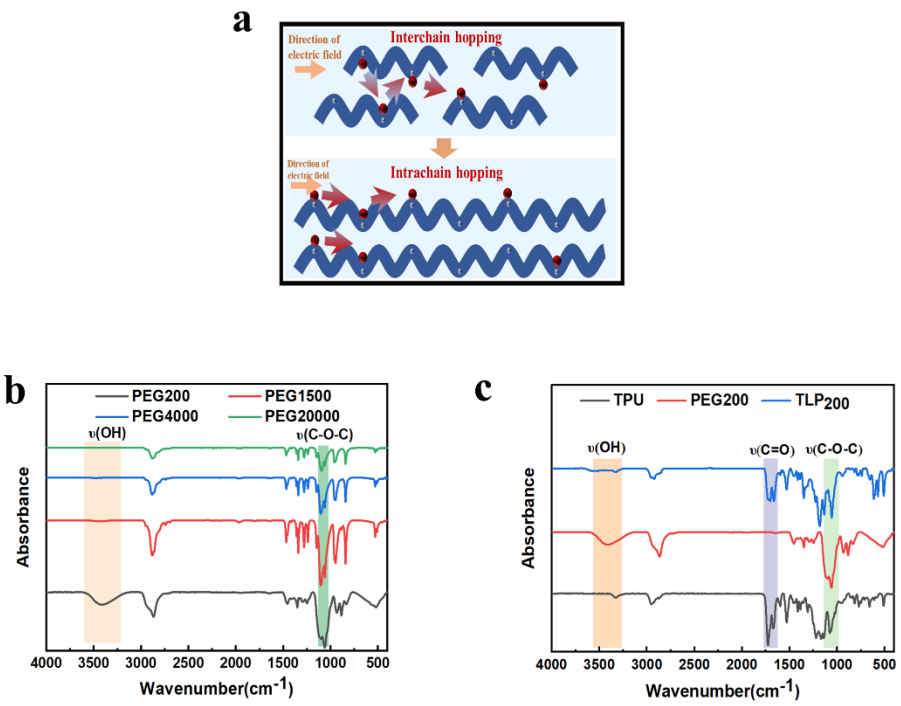

Fig. S3 (a) Mechanism of ion transport in ASSICEs. (b) ATR-FTIR spectra of various molecules weight of PEG. (c) ATR-FTIR spectra of various samples.

Fig. S3a shows the transport mode of lithium ion in elastomer polymer gradually changes from inter-chain transfer to intra-chain transfer with the increase of PEG chain. Fig. S3b shows characteristic peak of various molecule weight of PEG, -OH and C-O-C groups in the PEG_{200} are the most obvious, so we employed the PEG_{200} as an example to verify the successful construction of the ASSICEs. We can clearly observe the

disappearance of -OH, a distinct blue shift of C=O and C-O-C upon addition of lithium salt in Fig. S3c, implying that the coordination is formation between the C−O−C and C=O groups of the matrix network with Li^+ ions.

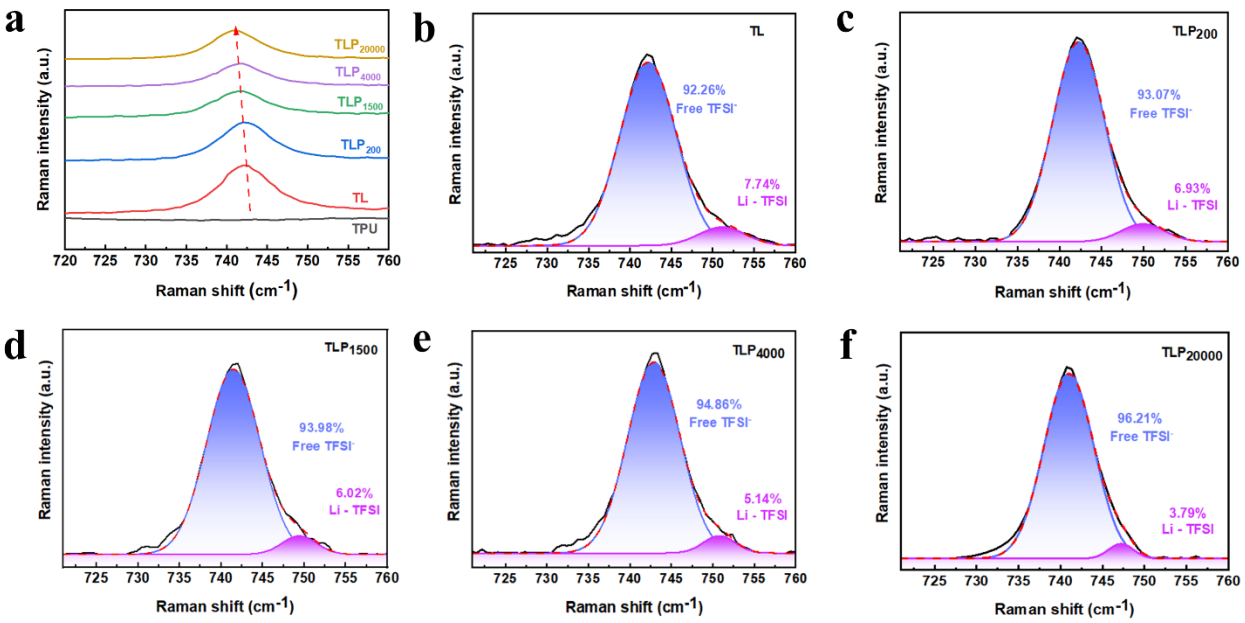

Fig. S4 (a) Raman spectra in the range of 720-760 cm^{-1} region corresponding to the breathing mode of $TFSI^-$, including pure TPU sample, TL, TLP_{200}, TLP_{1500}, TLP_{4000}, TLP_{20000}. (b ~ f) The relative percentage of free $TFSI^-$ and coordinate $TFSI^-$ with Li^+.

We have employed Raman spectroscopy to verify the hypothesis that multivalent ion-dipole interactions can increase the concentration of free ions. The most pronounced Raman band of the $TFSI^-$ anion, observed at approximately 740 cm^{-1}, originates from the collective expansion and contraction of the entire anion[29, 30]. This band exhibits the highest sensitivity (i.e., shift in band position) towards ionic association, and numerous studies have investigated variations in $TFSI^-$ - Li^+ cation coordination using this band[31-33]. Free $TFSI^-$ displays this band at 740 cm^{-1}, while coordination with Li^+ causes a shift to higher wavenumbers[7, 32, 34]. As shown in Fig. S4a, as the degree of PEG

polymerization increases, the characteristic band of $TFSI^-$ shifts from 742 cm^{-1} to 740 cm^{-1}, indicating enhanced polyvalent ion-dipole interactions in the system that promote lithium salt dissociation and significantly increase the proportion of free $TFSI^-$. Moreover, the validity of this observation is further reinforced by the analysis of relative area ratios obtained from Gaussian fitting peaks in Raman spectroscopy (Fig.S4b-S4f).

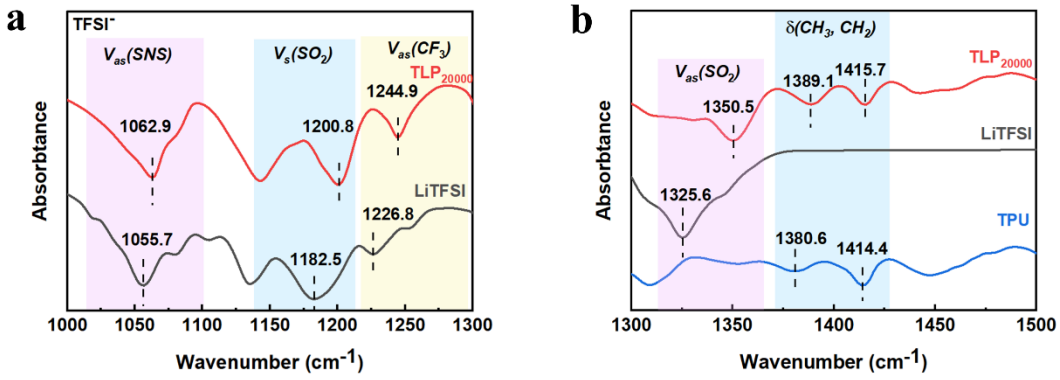

Fig. S5 ATR-FTIR characterization of TPU, LiTFSI and TLP_{20000} to verify polyvalent ion-dipole interaction. (a, b) The range of 1000-1440 cm^{-1} corresponds to the $TFSI^-$ stretching in TLP^{20000}, which can be attributed to the weakened Coulomb forces resulting from ion-dipole interactions affecting the Li ions.

In addition, we employed ATR-FTIR to investigate the polyvalent ion-dipole interactions between the O atoms of ASSICEs' skeleton and Li^+ of LiTFSI salts (Fig. S5). The antisymmetric stretching bond of S=O in $TFSI^-$ exhibits a shift from 1325.6 cm^{-1} to 1350 cm^{-1}, while the N-S antisymmetric stretching bond of $TFSI^-$ undergoes a shift from 1055.7 cm^{-1} to 1062.9 cm^{-1} (Fig. S5a, S5b) [29, 35]. The blue shift of the two bands indicates that the S=O and N-S bands are stronger[36, 37]. The electronegative oxygen within the ASSICEs' skeleton forms polyvalent ion-dipole interactions with lithium cations, thereby attenuating the Coulombic force between Li^+ cations and $TFSI^-$

anions in lithium salts. This leads to the enhanced electronegativity of N atoms within dissociated $TFSI^-$ anions[36]. Furthermore, the CH_3 and CH_2 bending vibration band blue shift from 1380.6, 1414.4 to 1389.1, 1415.7 cm^{-1}, respectively (Fig. S5b), indicating a weaker interaction between the H atoms in ASSICEs' skeleton and the F atoms of $TFSI^-$ anions[36]. The stretching of these bonds provides compelling evidence supporting the multivalence ion-dipole interactions formed between the O atoms in ASSICEs' skeleton and the Li^+ cations of LiTFSI salt. Additionally, the polyvalency of ion-dipoles has been confirmed by employing a molecular model to calculate the binding energy between Li^+ and PEG with varying degrees of polymerization using density functional theory (Table S3, S4, S5 and Fig. 4a, 4b and Fig. S17, S18, S19).

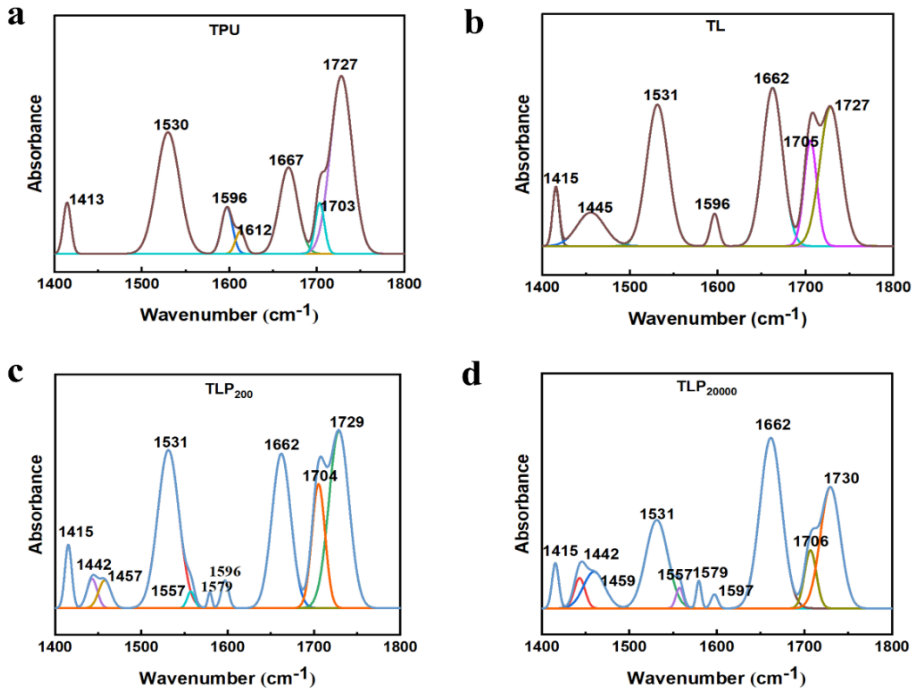

Fig. S6 ATR-FTIR spectra and the corresponding Gaussian fitting results of various samples in the range of 1400-1800 cm^{-1}, including the sample of pure TPU, TL, TLP_{200} and TLP_{20000}.

ATR-FTIR spectra was employed to deeper elucidate the interaction between

LiTFSI and the elastic matrix structure. The characteristic peak about 1530 cm^{-1}, 1667 cm^{-1}, 1703 cm^{-1} and 1727 cm^{-1} in the neat TPU is attributed to N-H deformation vibration, H-bonded C-N stretching and N-H deformation vibration, H-bonded C=O stretching vibration and free C=O stretching vibration, respectively [7]. Especially, the aromatic group absorbance peak of 1413 cm^{-1}, 1596 cm^{-1} and 1612 cm^{-1} is attributed to the C-H bending vibration, C=C skeleton vibration and stretching vibration (Fig. S6a).

When integration of LiTFSI or/and PEG, the emerging peak at 1445 cm^{-1} indicated that the hydrogen bonding donors in $TFSI^-$ and the free hydrogen bonding receptor N-H bonds generated a new interaction. The initial absorbance peaks at 1703 cm^{-1} and 1727 cm^{-1} in neat TPU of C=O groups are engaged in free stretching vibrations (Fig. S6a). Upon addition of a high concentration of LiTFSI, the free C=O stretching vibrations shift towards H-bonded C=O stretching vibrations (Fig. S6b). Subsequently, upon replacement of PEG_{200} with PEG_{20000}, the H-bonded C=O stretching vibrations recover back to free C=O stretching vibrations (Fig. S6c and S6d). These results suggest that the abundant dissociated Li^+ ions from LiTFSI can form Li-O bonds with the freely vibrating C=O groups; however, the presence of PEG hinders interaction between Li^+ ions and C=O by forming Li-O bonds with the C-O-C moieties within the PEG chains.

Combining ATR-FTIR spectra in Fig. 3d, Fig. S3, Fig. S4, Fig. S5 and Fig. S6, it can be proved that ASSICEs chemical structure can promote LiTFSI dissociation and Li^+ ions intrachain migration.

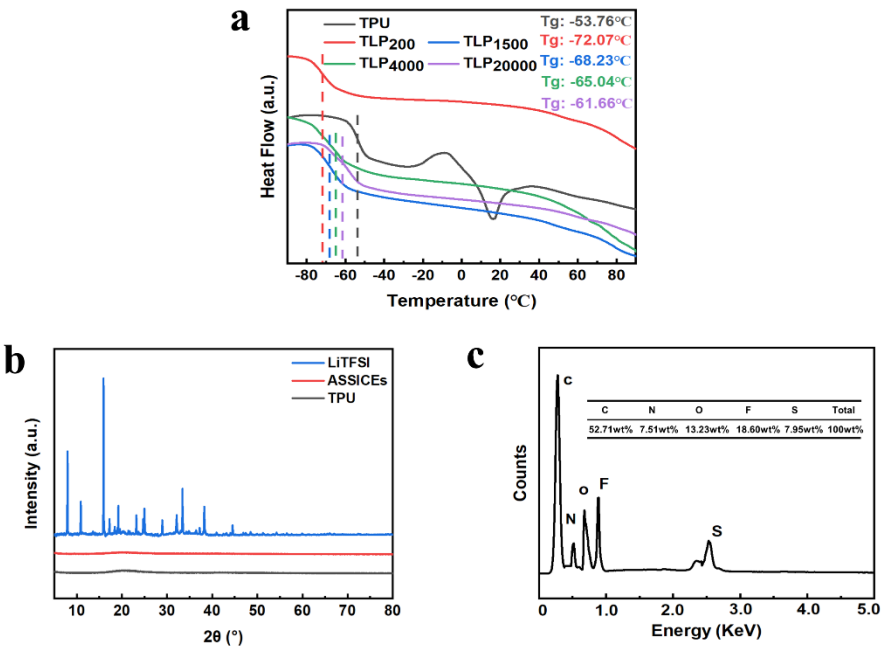

Fig. S7 (a) The DSC curves of various samples. (b) XRD patterns of TPU and ASSICEs. (c) Distribution diagram of elements (inset: the table of specific data).

The thermal properties of various samples were characterized by DSC. The DSC of polyurethane exhibit multiple peaks, which arise from the presence of both hard and soft segments [38]. The glass transition temperature values of the hard segment and soft segment of neat TPU are 18.00 ℃ and -53.76 ℃, respectively (Fig. S7a). when integrating the LiTFSI and PEG, the glass transition temperature peak of hard segments nearly disappeared and can hardly obtain the value, which suggest that the crystalline structure of TPU is destroyed by the lithium salts and PEG. But the glass transition temperature values of the soft segment are gradually increase as the increase of PEG molecule weight, from -72.07 ℃ increased to -61.66 ℃, which indicated more amorphous phases were formed. The phenomenon is consistent to the XRD results (Fig. S7b) and Element Mapping of SEM (Fig. S7c), these results indicated that the amorphous phase will beneficial to improve the ionic conductivity.

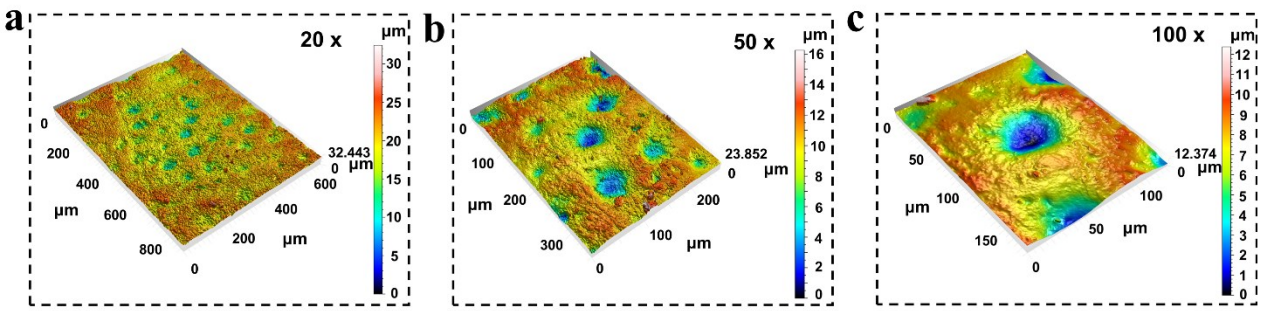

Fig. S8 Surface topography test of ASSICEs. (a) Surface topography magnified 20 ×. (b) Surface topography magnified 50 ×. (c) Surface topography magnified 100 ×.

Additionally, the 3D morphology of the ASSICEs' surface was measured using a laser confocal surface roughness measurement system to investigate the absence of a squeezing-out phenomenon akin to that observed in ionic liquids. As shown in Fig. S8, the surface of the sample exhibits the presence of sealed pores of diverse dimensions, resulting from the volatilization of solvent, a factor potentially augmenting mechanical toughness. However, no conspicuous evidence of a squeezing-out phenomenon is discernible.

Fig. S9 The photographs demonstrate that the ASSICEs exhibit a tensile strength of up to 1400% at a temperature of 50 ℃.

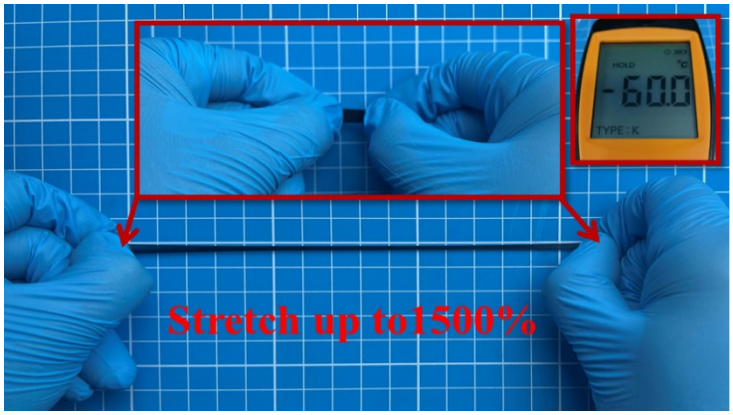

Fig. S10 The photographs demonstrate that the ASSICEs exhibit a tensile strength of up to 1500% at a temperature of -60 ℃.

The original sample is cut to a size of 20 ×5 mm and the surface of ASSICEs is painted black using an oil-based marker in to achieve a clearer display. The elastomer is subsequently subjected to a temperature of 50 ℃ or -60 ℃, causing the initial length of 10 mm to be extended to150 mm or 160 mm, the resulting strain is 1400% or 1500%. The observed phenomenon demonstrates that ASSICEs exhibit favorable mechanical properties even at a temperature of 50 ℃ or -60 ℃, showcasing their exceptional resilience to extremely ambient conditions. Consequently, the application is significantly broadened.

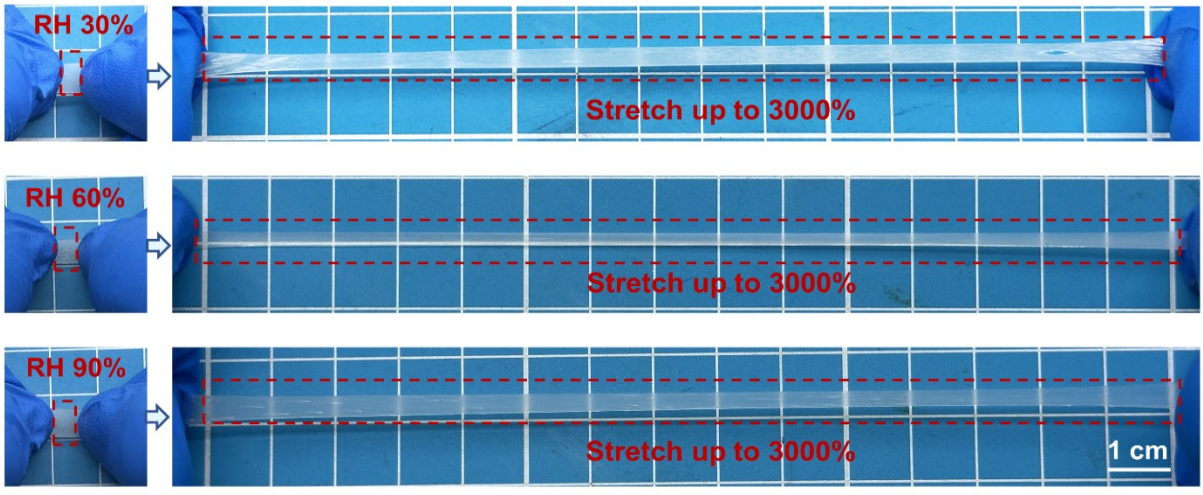

Fig. S11 Mechanical tensile properties of ASSICEs under varying humidity conditions.

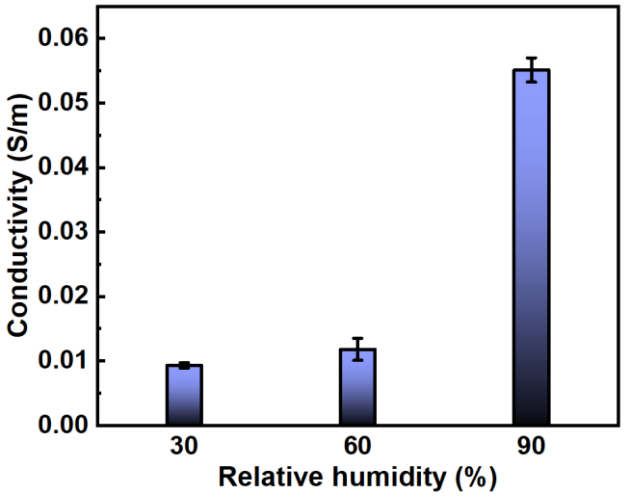

Fig. S12 Conductivity of ASSICEs under varying humidity conditions.

To investigate the impact of humidity fluctuations on the mechanical and electrical properties of ASSICEs, we initially subjected the samples to a controlled temperature and humidity environment for 24 hours, followed by conducting relevant tests. The ASSICEs exhibit exceptional mechanical stability, as illustrated in Fig. S11, and maintain their stretchability of up to 3000% even under varying relative humidity (RH) conditions. Furthermore, the conductivity is closely correlated with humidity; a slight increase in conductivity is observed as the humidity increases from 30% to 60%. Under high relative humidity conditions (RH90%), a significant increase in conductivity is noted, potentially attributed to the condensation of steam on the material surface (Fig. S12).

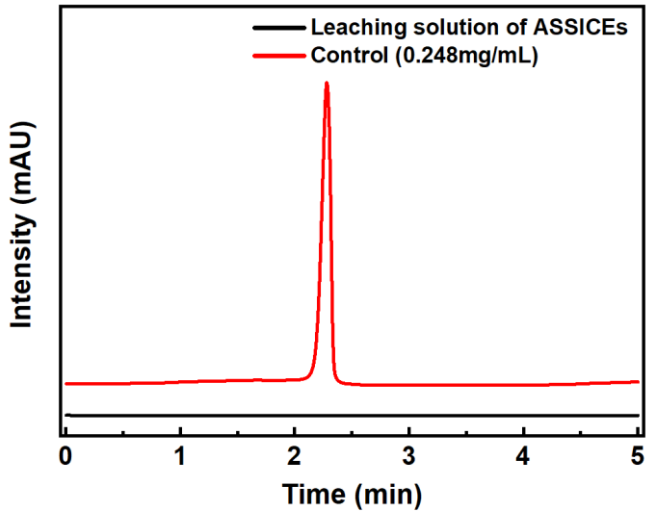

Fig. S13 The evaluation of residual DMF using HPLC.

We utilized high-performance liquid chromatography (HPLC) to assess the residual DMF. The DMF solution of the control exhibited a prominent absorption peak at 2.3 minutes, as depicted in Fig. S13. Conversely, such an absorption peak was absent in the leaching solution of the sample, indicating an almost negligible presence of residual DMF organic solvent in the ASSICEs.

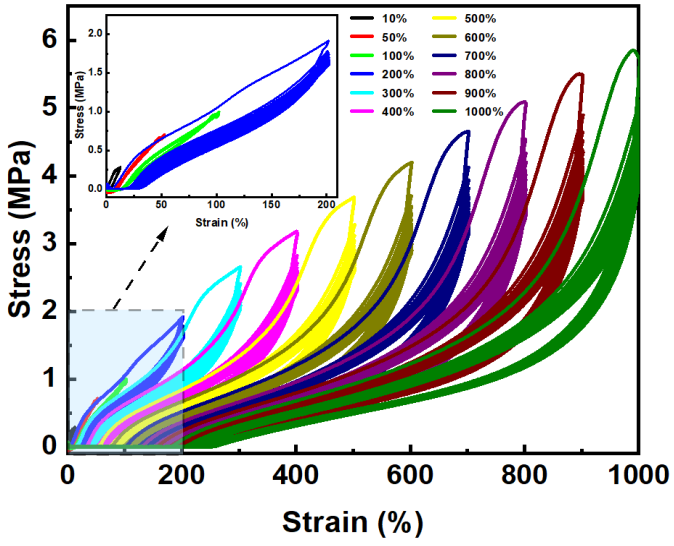

Fig.S14 Cyclic tensile curves of the ASSICEs with the predetermined strain increasing from 10% to 1000%.

To further investigate the elastic behavior of the ASSICEs, we have conducted a series of 30 stress-strain cycle experiments across varying strain levels. As shown in Fig. S14, our findings reveal minimal elastic hysteresis and exceptional elastic recovery properties within the test strain range of 0 to 1000%. These results demonstrate the elastomers' capability to fulfill diverse high-strain monitoring needs.

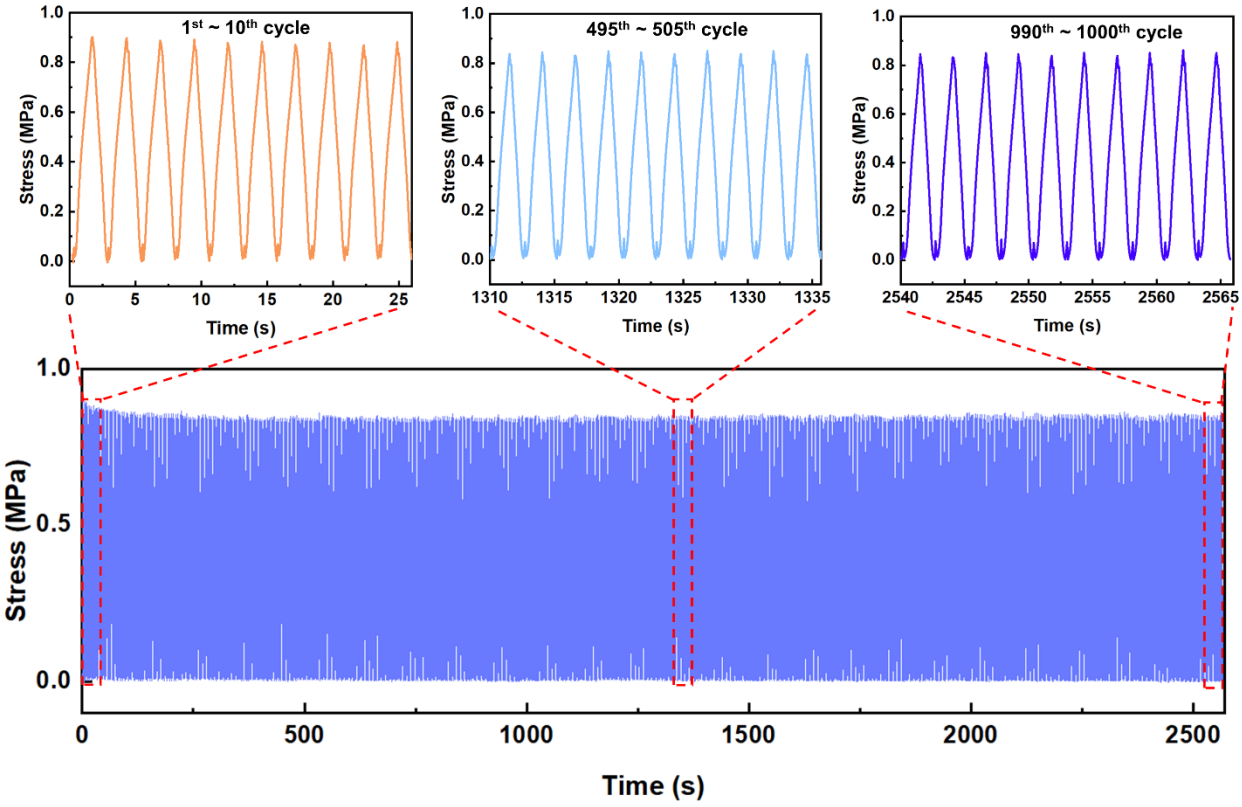

Fig. S15 Cyclic mechanical performance test of the ASSICEs under a strain of 100%.

To evaluate the mechanical stability of ASSICEs, we conducted cyclic mechanical stability tests (Fig. S15). The tests were performed under conditions of 100% tensile strain and a stretching rate of 200 mm/min. A total of 1000 loading/unloading cycles were employed. The magnified diagrams from three distinct intervals (1st~10th, 495th~505th, 990th~1000th cycles) consistently reveal a maximum stress value of approximately 0.8 MPa, indicating the exceptional mechanical stability of the ASSICEs.

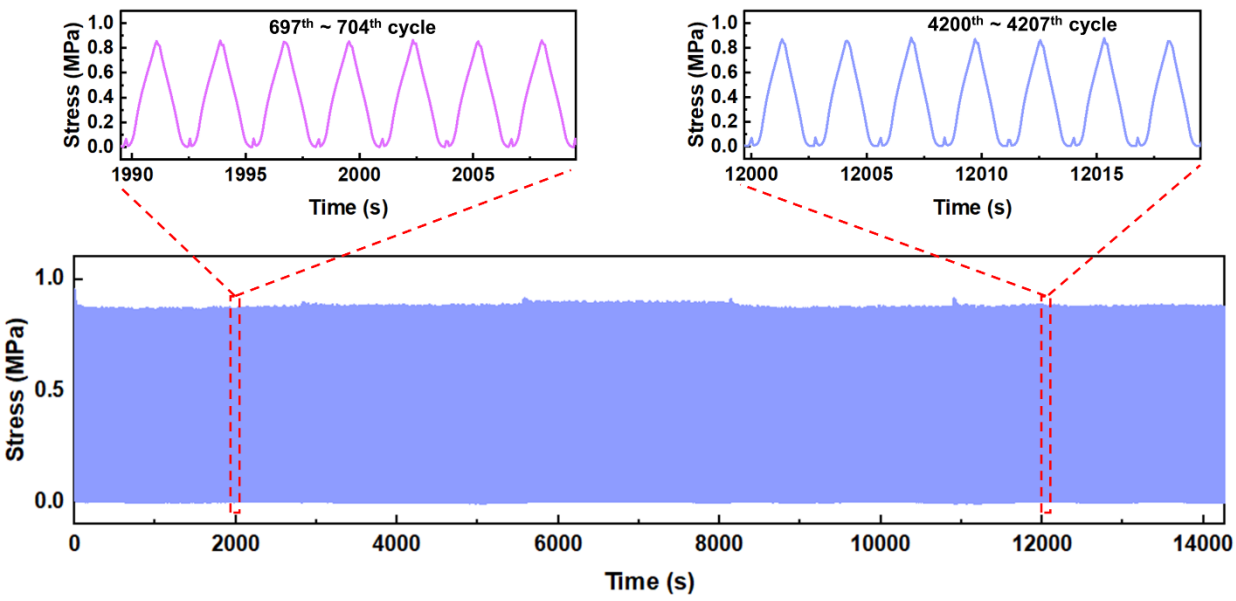

Fig.S16 Fatigue test of the ASSICEs under a strain of 100%.

To investigate the durability of ASSICEs in practical applications, we conducted fatigue tests, subjecting the materials to up to 5000 load/unload cycles at a strain of 100% and a stretching rate of 200 mm/min (Fig. S16). The magnified diagrams of two different periods (697th~704th, 4200th~4207th) reveal a consistent maximum stress value of approximately 0.8 MPa, indicating the exceptional fatigue resistance of the ASSICEs.

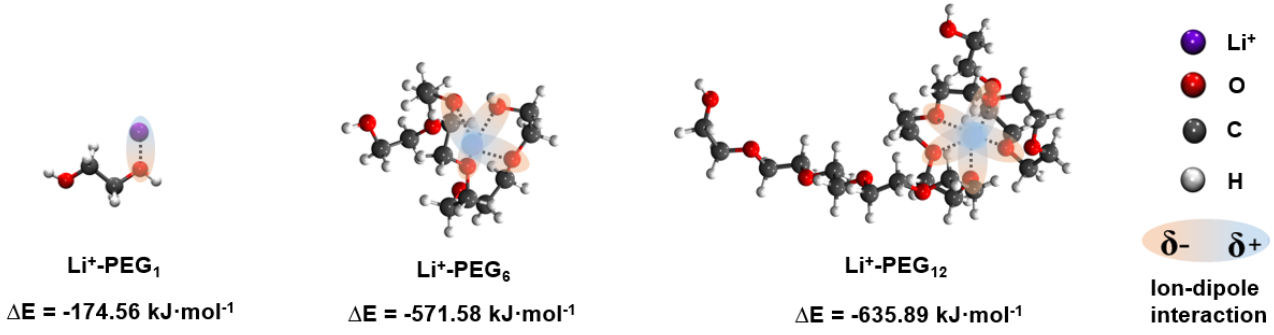

Fig. S17 The binding energy between Li^+ and single PEG molecule with varying degrees of polymerization was calculated using the density functional theory (DFT).

To gain further insight into the interaction between Li^+ and single PEG molecule with varying degrees of polymerization, we carried out density functional theory

calculations (Fig. S17). The DFT analysis revealed the emergence of multivalent ion-dipole interactions with an increase in the polymerization degree of PEG, leading to a corresponding enhancement in the binding energy of Li^+-ether/Li^+-ester ion-dipole interactions.

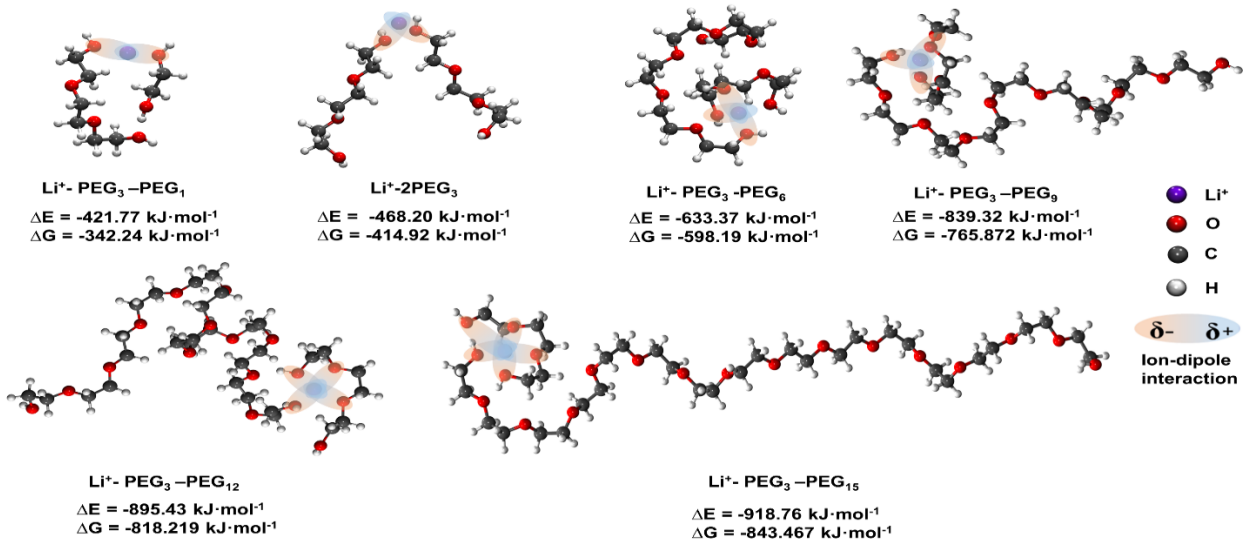

Fig. S18 The binding energy and Gibbs free energy between Li^+ and 2 PEG molecules with varying degrees of polymerization.

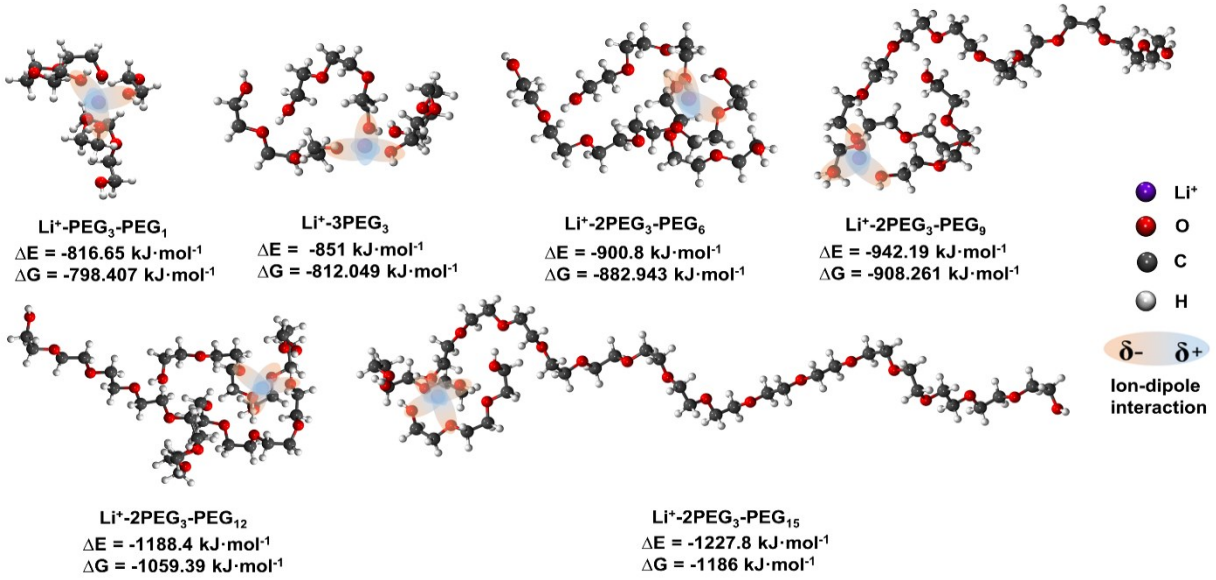

Fig. S19 The binding energy and Gibbs free energy between Li^+ and 3 PEG molecules with varying degrees of polymerization.

In addition, to verify the multivalent ion-dipole interactions of Li^+-ether, we performed additional calculations using DFT to assess the interaction energies between Li^+ and multiple PEG molecules, such as 2 or 3 PEG molecules. The calculation results, as depicted in Fig. S18 and S19, demonstrate that the binding energy and Gibbs free energy continue to increase with the degree of polymerization in the presence of multiple PEG molecules. Additionally, the entropy values (Table S4 and S5) also follow this pattern.

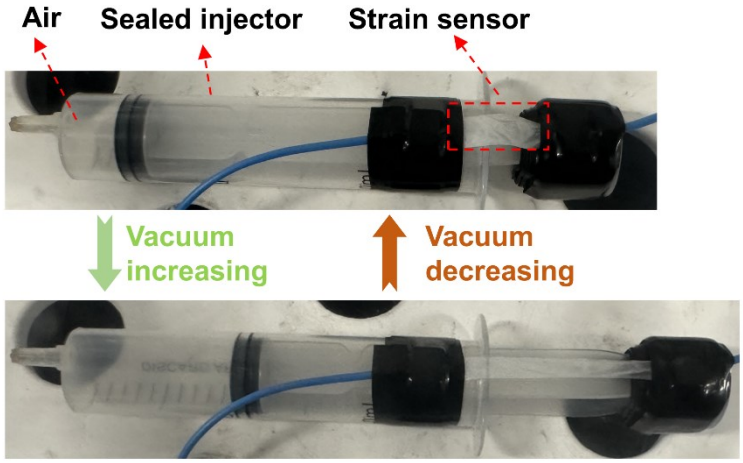

Fig S20 Photograph of a vacuum measuring device.

A proof-of-concept assessment for vacuum degree testing was conducted using the device (Fig. S18, Movie S3), demonstrating that ASSICEs exhibit the capability to deliver precise vacuum degree measurements. This proficiency is attributed to their outstanding mechanical and electrical properties, coupled with environmental robustness.

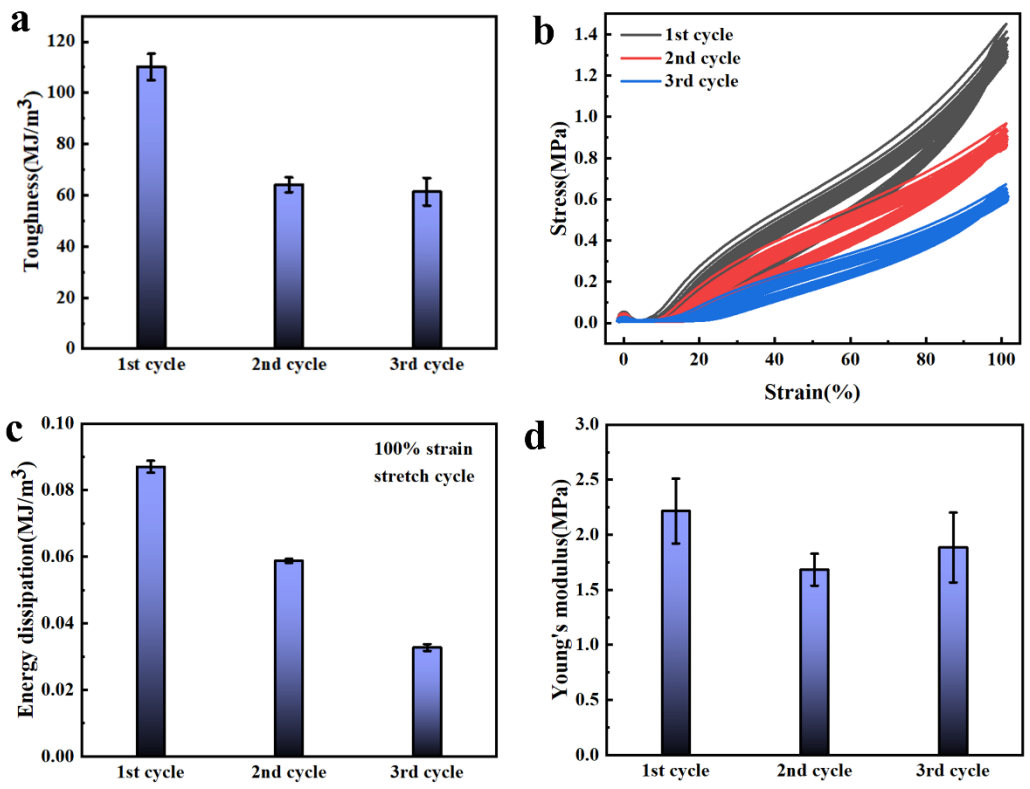

Fig. S21 (a) Toughness of recyclable samples. (b) Stress-strain cycle curve of recyclable samples. (c) Energy dissipation of recyclable samples. (d) Yong's modulus of recyclable samples.

Mechanical properties of recycled samples are comprehensive evaluated in Fig. S21. After the third recycling, the mechanical properties of the samples experience a slight decrease and subsequently stabilize. However, this decline does not have a significant impact on their practical applications.

4. List of Movies

Movie S1. Dynamic stretching demonstration video at room temperature.

Movie S2. Load-bearing dynamic demonstration video.

Movie S3. Vacuum measurement demonstration video.

5. References

1. A. D. Becke, *Phys Rev A Gen Phys*, 1988, **38**, 3098-3100.
2. C. Lee, W. Yang and R. G. Parr, *Phys. Rev., B Condens. Matter*, 1988, **37**, 785-789.
3. S. Grimme, J. Antony, S. Ehrlich and H. Krieg, *J. Chem. Phys.*, 2010, **132**, 154104.
4. C. T. Lee, W. T. Yang and R. G. Parr, *Physical Review B*, 1988, **37**, 785-789.
5. W. Humphrey, A. Dalke and K. Schulten, *J. Mol. Graph. Model.*, 1996, **14**, 33-38.
6. M. Kröger, J. D. Dietz, R. S. Hoy and C. Luap, *Computer Physics Communications*, 2023, **283**, 108567.
7. J. Chen, X. T. Deng, Y. Y. Gao, Y. J. Zhao, X. P. Kong, Q. Rong, J. Q. Xiong, D. M. Yu and S. J. Ding, *Angew. Chem. Int. Ed.*, 2023, **62**, 202307255.
8. L. Peng, L. Hou and P. Y. Wu, *Adv. Mater.*, 2023, **35**, 2211342.
9. H. Xiang, X. X. Li, B. H. Wu, S. T. Sun and P. Y. Wu, *Adv. Mater.*, 2023, **35**, 2209581.
10. W. W. Niu, Q. Tian, Z. Y. Liu and X. K. Liu, *Adv. Mater.*, 2023, **35**, 2304157.
11. H. C. Wang, Q. Wang, X. Cao, Y. Y. He, K. Wu, J. J. Yang, H. H. Zhou, W. Liu and X. M. Sun, *Adv. Mater.*, 2020, **32**, 2001259.
12. J. Lopez, Y. M. Sun, D. G. Mackanic, M. Lee, A. M. Foudeh, M. S. Song, Y. Cui and Z. N. Bao, *Adv. Mater.*, 2018, **30**, 1804142.
13. L. Y. Wang, Y. Wang, S. Yang, X. M. Tao, Y. L. Zi and W. A. Daoud, *Nano Energy*, 2022, **91**, 106611.
14. B. R. B. Yiming, Y. Han, Z. L. Han, X. N. Zhang, Y. Li, W. Z. Lian, M. Q. Zhang, J. Yin, T. L. Sun, Z. L. Wu, T. F. Li, J. Z. Fu, Z. Jia and S. X. Qu, *Adv. Mater.*, 2021, **33**, 2006111.
15. X. Qu, W. Niu, R. Wang, Z. Li, Y. Guo, X. Liu and J. Sun, *Mater. Horiz.*, 2020, **7**, 2994-3004.
16. M. Y. Yao, B. H. Wu, X. D. Feng, S. T. Sun and P. Y. Wu, *Adv. Mater.*, 2021, **33**, 2103755.
17. L. Shi, T. X. Zhu, G. X. Gao, X. Y. Zhang, W. Wei, W. F. Liu and S. J. Ding, *Nat. Commun.*, 2018, **9**, 2630.
18. J. Chen, Y. Gao, L. Shi, W. Yu, Z. Sun, Y. Zhou, S. Liu, H. Mao, D. Zhang, T. Lu, Q. Chen, D. Yu and S. Ding, *Nat. Commun.*, 2022, **13**, 4868.
19. P. P. Zhang, W. B. Guo, Z. H. Guo, Y. Ma, L. Gao, Z. F. Cong, X. J. Zhao, L. J. Qiao, X. Pu and

Z. L. Wang, *Adv. Mater.*, 2021, **33**, 2101396.

20. W. L. Qiu, C. G. Zhang and Q. Zhang, *ACS Appl. Mater. Interfaces*, 2022, **14**, 42578-42585.
21. C. C. Li, J. X. Cheng, Y. F. He, X. N. He, Z. Y. Xu, Q. Ge and C. H. Yang, *Nat. Commun.*, 2023, **14**, 4853.
22. W. J. Xia, Y. J. Yu, C. J. Zhou, W. J. Wang, Z. Q. Wu and H. Chen, *J. Mater. Chem. C*, 2023, **11**, 16545-16553.
23. C. Zhou, X. Song, W. Xia, S. Liu, Z. Wu and H. Chen, *Chem. Eng. J.*, 2024, **489**, 151433.
24. Q. R. Wu, Y. D. Xu, S. J. Han, J. D. Zhu, A. B. Chen, J. Y. Zhang, Y. J. Chen, X. X. Yang, J. R. Huang and L. H. Guan, *Mater. Horiz.*, 2023, **10**, 3610-3621.
25. P. Shi, Y. Wang, K. Wan, C. Zhang and T. Liu, *Adv. Funct. Mater.*, 2022, **32**, 2112293.
26. L. L. Ma, J. X. Wang, J. M. He, Y. L. Yao, X. D. Zhu, L. Peng, J. Yang, X. R. Liu and M. N. Qu, *J. Mater. Chem. A*, 2021, **9**, 26949-26962.
27. C. Dang, F. Zhang, Y. H. Li, Z. X. Jin, Y. B. Cheng, Y. F. Feng, X. J. Wang, C. Z. Zhang, Y. A. Chen, C. Y. Shao, Q. B. Zheng and H. S. Qi, *Small*, 2022, **18**, 2200421.
28. W. K. Xu, T. Shen, Y. T. Ding, H. J. Ye, B. Z. Wu and F. Chen, *Small*, 2024, 202310072.
29. I. Rey, P. Johansson, J. Lindgren, J. C. Lassègues, J. Grondin and L. Servant, *Journal of Physical Chemistry A*, 1998, **102**, 3249-3258.
30. M. Herstedt, M. Smirnov, P. Johansson, M. Chami, J. Grondin, L. Servant and J. C. Lassègues, *J. Raman Spectrosc.*, 2005, **36**, 762-770.
31. D. M. Seo, P. D. Boyle, R. D. Sommer, J. S. Daubert, O. Borodin and W. A. Henderson, *J. Phys. Chem. B*, 2014, **118**, 13601-13608.
32. D. Brouillette, D. E. Irish, N. J. Taylor, G. Perron, M. Odziemkowski and J. E. Desnoyers, *Physical Chemistry Chemical Physics*, 2002, **4**, 6063-6071.
33. D. M. Seo, O. Borodin, S. D. Han, P. D. Boyle and W. A. Henderson, *Journal of the Electrochemical Society*, 2012, **159**, A1489-A1500.
34. V. Nilsson, D. Bernin, D. Brandell, K. Edström and P. Johansson, *ChemPhysChem*, 2020, **21**, 1166-1176.
35. R. S. Talaty E R, Storhaug V J, et al. , *The Journal of Physical Chemistry B*, 2004, **108**, 13177-13184.

36. Y. C. Zhang, M. X. Li, B. Qin, L. L. Chen, Y. C. Liu, X. Zhang and C. Wang, *Chem. Mater.*, 2020, **32**, 6310-6317.
37. E. K. Boahen, B. Pan, H. Kweon, J. S. Kim, H. Choi, Z. Kong, D. J. Kim, J. Zhu, W. B. Ying, K. J. Lee and D. H. Kim, *Nat. Commun.*, 2022, **13**, 7699.
38. S. S. Wang and K. Min, *Polymer*, 2010, **51**, 2621-2628.